

**GT2011-46109**

## **VALIDATION OF NUMERICAL SIMULATION FOR ROTATING STALL IN A TRANSONIC FAN**

**Minsuk Choi<sup>1</sup>, Nigel H. S. Smith<sup>2</sup> and Mehdi Vahdati<sup>1</sup>**

<sup>1</sup>Imperial College London, London, UK

<sup>2</sup>Rolls-Royce PLC, Derby, UK

### **ABSTRACT**

This paper addresses a comparison of numerical stall simulations with experimental data at 60% (subsonic) and 95% (supersonic) of the design speed in a modern transonic fan rig. The unsteady static pressures were obtained with high frequency Kulite transducers mounted on the casing upstream and downstream of the fan. The casing pressure variation was clearly visible in the measurements when a stall cell passed below the transducers. Numerical stall simulations were conducted using an implicit, time-accurate 3D compressible RANS solver. The comparisons between the experiment and simulation mainly cover performance curves and time-domain pressure traces of Kulites during rotating stall. At two different fan speeds, the stall characteristics such as the number and rotating speed of the stall cells were well-matched to the experimental values. The mass flow rate and the loading parameter under the fully-developed rotating stall also showed good agreement with the experiment. In both numerical and experimental results, a large stall cell was eventually formed after stall inception regardless of the fan speed. Based on the validation, the detailed flow has been evaluated to understand rotating stall in a transonic fan. In addition, it was found that the mass flow measurement using casing static pressure might be wrong during transient flow if the Kulites were mounted too close to the fan blade.

### **INTRODUCTION**

Avoiding rotating stall in operation is one of the most important issues for fan designer. Since rotating stall can cause a performance reduction and it is potentially a very serious threat to engine integrity, attention has been focused on understanding the physical mechanisms of it. Due to modeling difficulties, much of the stall research is experimental and focuses on stall inception and its suppression [1-5]. Based on these experimental results, it was found that rotating stall follows either long-length (modal) or short-length (spike)

waves depending on compressor operating conditions. In particular, Camp and Day [3] found that a spike-type stall inception is connected to a three-dimensional local flow instability while a modal oscillation is a two-dimensional disturbance; they proposed a simple model based on the slope of the characteristics to explain the type of stall inception. In computational research, most rotating stall simulations are conducted using simplified or partial geometries [6-10] but large-scale numerical simulations, including whole geometries, are beginning to emerge and give an understanding into rotating stall [11-15]. As an example, based on their numerical results, Vo et al. [10] proposed two criteria for the occurrence of spike-type rotating stall, namely tip clearance flow spillage at the leading edge and tip clearance back flow at the trailing edge. Vahdati et al. [11] have successfully simulated the unsteady flow and aeroelasticity behavior of a core compressor during rotating stall and surge. However, although these numerical results can provide some intuitive understanding of rotating stall characteristics, there is a shortage of reliable experimental data for validating stall simulation results. Most researchers use steady experimental data for validating their numerical results and assume their flow solver to perform reasonably well under rotating stall (In fact, calculation appears to be reasonably good at predicting number and speed of stall cells). Recently, Gourdain et al. [15] published a paper comparing their numerical results to the experimental ones in a subsonic compressor. They correctly estimated the stall-margin but obtained a different stall pattern (number of cells, cell speed and flow blockage) from the experiment, and also failed to obtain the correct mass flow rate under rotating stall. They suggested methods that can improve the accuracy of stall simulations based on their numerical results.

Choi et al. [13-14] have been trying to simulate rotating stall as realistically as possible. The present work is a continuation of their stall studies. Therefore, this paper focuses on a comparison of rotating stall between experiment and

numerical simulation and evaluates the capability of numerical methods and boundary conditions for stall simulations.

## TEST FACILITY AND DATA ACQUISITION

A research fan was tested in a 34-inch diameter fan rig with an engine-representative bypass ratio. The rig had separate throttles for the bypass and core streams; each stream had stators to remove the swirl from the fan. The fan blade tested was a typical wide chord fan blade at 26-off with a relative tip Mach number of 1.4. The facility is typically used to measure steady state performance data and to map the stall drop-in and drop-out boundaries of the fan.

During operation of the facility, constant speed characteristics were mapped out by throttling the bypass to the stability boundary while the core stream was set to a fixed throttle position. Three rings of Kulites were mounted on the casing approximately half an axial chord upstream and downstream of the fan leading and trailing edge, and in the bypass duct downstream of the outlet guide vane. Unsteady data were acquired during each stability event: a complete stall hysteresis at 60% and 95% speeds including stall inception, development and recovery. Data from the Kulites were sampled at a frequency of 2.5kHz, so only the bulk fluctuation generated by the stall cell could be captured, but not those produced by the blade passing. These data were also used to calculate the overall performance of the test rig during stall cycles. At each axial location, 6 Kulites were used to measure unsteady pressure; the exact circumferential position of the Kulites upstream and downstream of the fan is shown in **Table 1**. A more detailed description of experimental setup can be found in Anderson and Smith [16].

## NUMERICAL METHOD

### Flow Model

An implicit, time-accurate 3D compressible RANS solver was used throughout the study. This flow solver is based on a cell-vertex finite volume methodology and mixed-element unstructured grids. The mesh is characterized using an edge-based data structure and the grid is presented to the solver as a set of node pairs connected by edges. The central differencing scheme is applied with a mixture of second- and fourth-order matrix artificial dissipation for stabilization. In addition, a pressure switch, which guarantees that the scheme is total variation diminishing and reverts to a first-order Roe scheme in the vicinity of discontinuities, is used for numerical robustness. The resulting semi-discrete system of equations is advanced in time using a point-implicit scheme with Jacobi iteration and dual time stepping. Solution acceleration techniques, such as residual smoothing and local time stepping, are employed for steady-state flow calculations. For unsteady computation, an outer Newton iteration procedure is used where the time steps are dictated by the physical restraints and remain fixed through the solution domain. Within a Newton iteration, the solution is advanced to convergence using previously-mentioned

**Table 1 Location of Kulites**

| Axial location           | 50% $C_x$ upstream of fan        | 50% $C_x$ downstream of fan       |
|--------------------------|----------------------------------|-----------------------------------|
| Circumferential position | 30°, 90°, 131°, 207°, 306°, 353° | 7.5°, 61°, 122°, 152°, 222°, 304° |

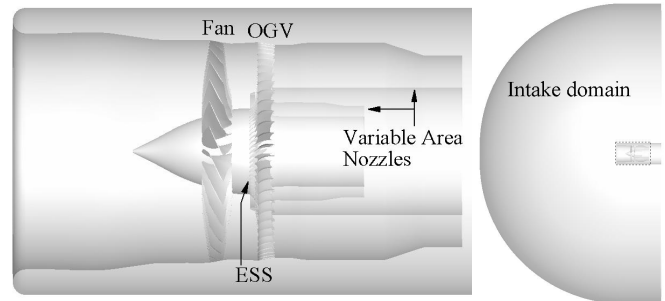


**Fig. 1 Computational domain**

acceleration techniques. Further details can be found in Sayma et al. [17]. For reference, 1200 time steps per fan revolution were used in the stall simulations.

### Computational domain and Boundary Conditions

Based on the real geometry of the fan rig, the computational geometry was reconstructed as shown in **Fig. 1**. The domain includes a whole-annulus fan assembly with one mis-staggered blade, outlet guide vanes (OGVs) and engine section stators (ESSs); the fan is also modeled with a typical rig tip clearance. To enable the use of atmospheric boundary conditions, a large upstream region and two variable-area nozzles are also included in the computational domain. The variable-area nozzle, placed downstream of the OGVs, is adjusted to move the fan operating point, while the nozzle behind the ESSs is not changed in this study. All interface boundaries between moving and stationary bladerows were modeled using sliding planes. The whole computational domain has about 20 million nodes.

It is usual to specify the total pressure, total temperature, and flow angles at the inlet and the static pressure at the exit. However, for flows under rotating stall, obtaining reliable and accurate boundary conditions is difficult: Since the compressor is operating far from its design point, the flow upstream and downstream is non-uniform and the downstream boundary condition must be far from the fan. Moreover, the imposition of time-invariant exit static pressure is not valid, because the flow becomes unsteady during stall. An alternative way is to include a large intake domain for inlet and variable-area nozzle for outlet. Hence, only the ambient air conditions need to be specified at the inlet. A downstream variable-area nozzle allows the pressure behind the fan to adjust automatically, while the pressure behind the nozzle is fixed, as discussed in Vahdati et al. [18]. The nozzle area determines the equilibrium operating point between the mass flow and the pressure into it. For a choked nozzle, the solution is independent of the prescribed

boundary conditions at the nozzle exit and, for an unchoked nozzle, a uniform steady static pressure will suffice. With such an approach, no flow quantity is fixed at the exit and a powerful natural boundary condition is provided for stall simulations.

## NUMERICAL RESULTS

### Performance Curves

Before analyzing flow data, it is worth noting there are some differences in triggering rotating stall between the experiment and computation. In the experiment, the on-set of the rotating stall was achieved by throttling the bypass duct at constant speed, resulting in the fan operating further up its characteristic. The throttle was continually closed until the fan dropped into rotating stall; once data had been captured, the fan was recovered by quickly opening the bypass valve. In most numerical stall simulations, the exit pressure is increased to move the operating point over the stall line. However, the exit pressure increase, achieved by closing the nozzle, can cause large non-physical overshoots in the performance curves (Choi et al. [13]). In order to remedy the numerical overshoot, they suggested a two-step procedure for stall triggering [14]. It is important to obtain the near-stall conditions as close to the stall line as possible. Thereafter, a blade is mis-staggered by opening it by 0.5 degree and the stall computation begins with a minimal closing of the nozzle. The flow is impaired by the introduction of the mis-staggered blade and stall initiates. In this study, the same procedure was used to get an initial asymmetric disturbance for triggering rotating stall.

The mass flow rate versus pressure characteristics for the fan are shown in **Fig. 2**, during rotating stall at 60% and 95% speed. The abscissa represents the normalized mass flow rate divided by the choked mass flow rate at the design speed. The loading parameter is  $\Delta h/U^2$  in the ordinate. If we assume the process is isentropic after starting from the thermodynamic relationship, then the following equation can be obtained.

$$\Delta h/U^2 \approx \gamma RT_0 \left[ \left( \frac{p}{P_0} \right)^{(\gamma-1)/\gamma} - 1 \right] / [(\gamma-1)U^2] \quad (1)$$

The mass flow rate in the experiment was indirectly calculated using the isentropic relation with the casing static pressure and inlet total pressure, assuming that the flow field is uniform. However, in the numerical simulation, the mass flow rate ( $m_r$ ) is computed directly by using mass flux upstream of the fan. With  $m_r$ , the steady calculation results show a good agreement with the experimental data. The near-stall condition at 95% speed coincides with the experimental point, although the last stable point at 60% speed doesn't reach the near-stall point of the experiment. The near-stall points are used as initial conditions, and unsteady stall simulations commence by mis-staggering one of the fan blades in the assembly by 0.5 degree. It can be seen from **Fig. 2** that, at 95% speed, the mass flow and  $\Delta h/U^2$  decrease simultaneously and reach minimum values of 0.7 and 0.01 respectively. From this point, two values increase until they converge to their quasi-stable point

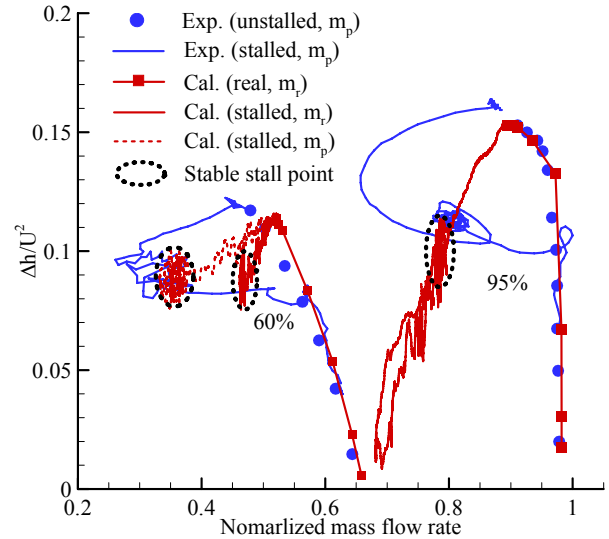


**Fig. 2 Performance curves**

(indicated by a black, dotted circle). The numerical locus of  $\Delta h/U^2$  for the transient flow from the near-stall condition to the quasi-stable stall point is different from the experiment, although both mass flow rate and  $\Delta h/U^2$  have a good agreement with the experimental values at the beginning and at the end. This is due to fact that, during the stall simulation at 95% speed, a strong reversal flow appears near the casing just after stall initiation and disappears quickly (in two fan revolutions), resulting in an excessive decrease of  $\Delta h/U^2$  during this transient period. It is unclear whether this reversal flow arises from a physical phenomenon or a numerical instability, and the authors have not succeeded in removing this phenomenon from their numerical simulations. However, as will be seen later, only a weak reversal flow appears just after stall inception at 60% speed where the flow is subsonic. This opens the question of whether the strength of reversal flow is related (physically or numerically) to the existence of shock waves. It should be noted that the fan is still capable of producing total pressure rise, about 88% of its peak value in mass-averaged total pressure ratio, during its transient although  $\Delta h/U^2$  approaches zero. This implies the stall region remains very close to the casing.

At 60% fan speed, there is no strong reversal flow so mass flow rate and  $\Delta h/U^2$  decrease steadily to the stable stall point. However, there seems to be a big difference in the mass flow rate between experimental and numerical results at 60% speed. However, this difference is only due to fact that the approach used to extract the mass flow rate from experimental data is different to the one used in numerical computations. If the mass flow rate ( $m_p$ ) is calculated from the numerical data using the same method as in the experiment, the fully-developed stall point at 60% fan speed becomes well-matched with experiment (as indicated with a red dotted line in **Fig. 2**). At 95% speed,  $m_p$  at stall point is similar to  $m_r$  with errors less than 10%. The difference between  $m_p$  and  $m_r$  during stall process will be discussed later.

### Pressure Histories

The static pressure time history on the casing will be used to compare numerical results with experimental data and to check the stall characteristics. There are six upstream Kulites that measure the unsteady pressure in the experiment. The calculations were used to create the equivalent of six numerical sensors on the casing at the same axial and circumferential positions as the experimental Kulites. It should be noted that the numerical data have been smoothed to remove high-frequency fluctuations caused by the blade passing.

**Figure 3** shows static pressure time histories on the casing at 50% axial chord upstream of the fan for 60% speed. Here, the revolutions in the computation start from the beginning of the unsteady calculation, while those in the experiment were shifted for the histories to look similar to the numerical ones. In the experiment, a growing stall cell is clearly visible around 5 revolutions and several cells appear around 7 revolutions. After 10 revolutions, a stable rotating stall with a large cell is formed which keeps its pattern for another 100 revolutions. Even before the stall cell's emergence, small asymmetric disturbances are clearly seen in the histories and are rotating with nearly the same speed as the fan rotor. The pressure histories extracted from the numerical data look similar to the experimental ones. For the first five revolutions, small ticks

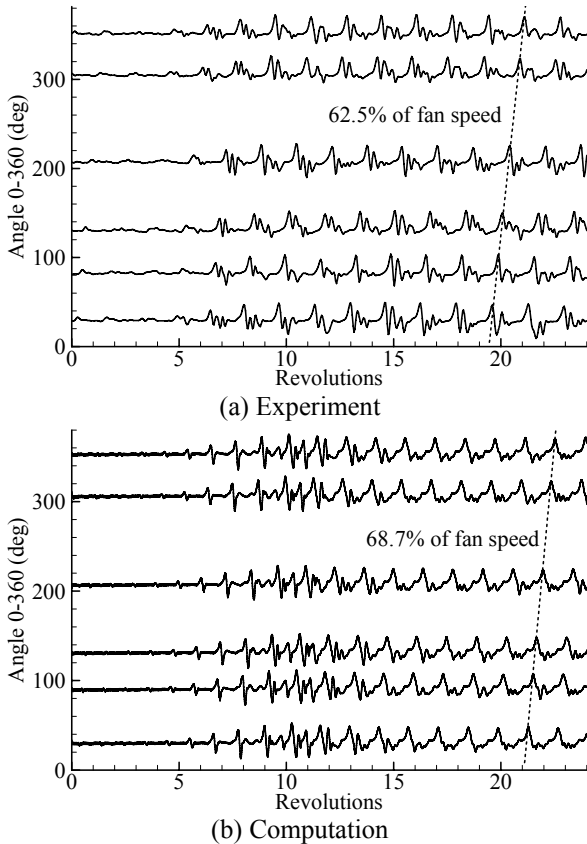


**Fig. 3** Static pressure time history at six numerical sensors located 50% axial chord upstream of fan for 60% speed

with small length scales (of a few blades), which are generated by the mis-staggered blade, exist in the flow. After 5 revolutions, a stall cell grows from the mis-staggered blade and propagates along the fan blade row, with a decreasing rotational speed in an absolute frame. Due to the movement of the first cell, several small cells appear at around 10 revolutions, and the rotating stall changes to a single large stall cell after 12 revolutions. After rotating stall is fully-developed, the shape of the time histories is well-matched to those in the experiment, and a specific pattern variation appears. As a stall cell passes the sensor, it causes a high-pressure peak followed by a low-pressure trough. The speed of the stall cell and the amplitude of pressure fluctuations are also comparable to each other.

At 95% speed as shown in **Fig. 4**, stall inception and development are similar to the 60% speed case. Some small disturbance appears for the first three revolutions in the experiment, followed by a growing stall cell. Just after stall initiation, many stall cells are found at around 5 revolutions which develop to a single large stall cell. In the numerical simulation, a stall cell originates from the mis-staggered blade at around 3 revolutions which has a similar shape to the experimental one at inception. There are some small disturbances present even before stall initiation. After another 5 revolutions, the rotating stall with a single stall cell is formed,

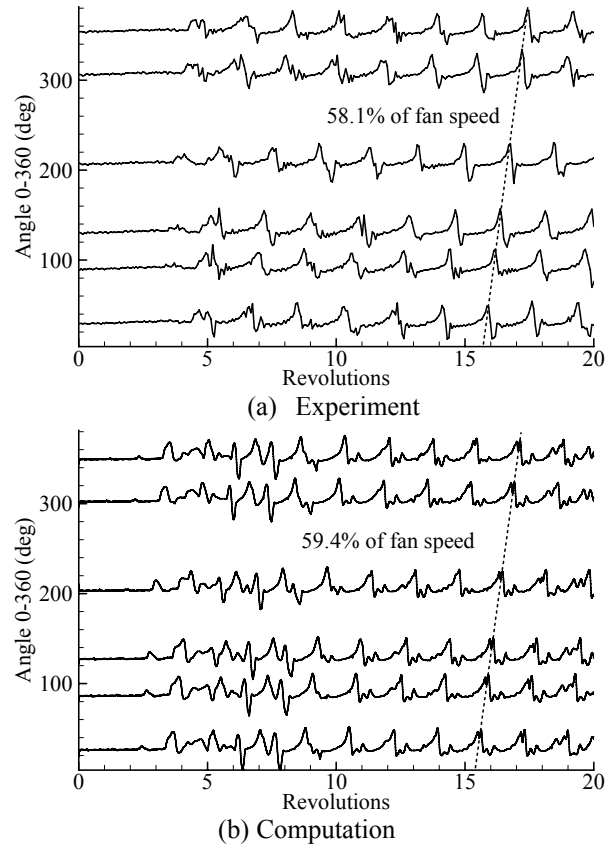


**Fig. 4** Static pressure time history at six numerical sensors located 50% axial chord upstream of fan for 95% speed

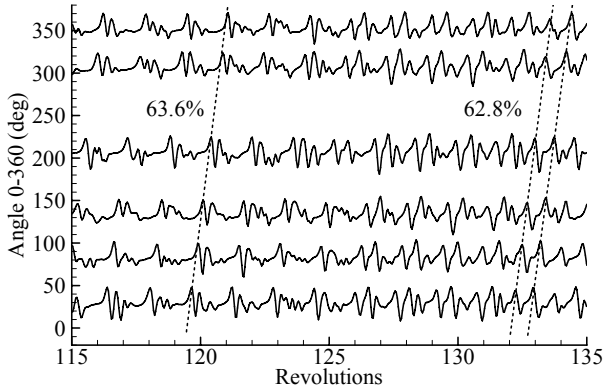


**Fig. 5 Static pressure time history at 60% speed**

**Table 2 Flow quantities under fully-developed rotating stall**

|                         | 60%       |            | 95%         |            |
|-------------------------|-----------|------------|-------------|------------|
|                         | Exp       | Cal        | Exp         | Cal        |
| $m_p$                   | 0.28~0.38 | 0.32~0.37  | 0.77~0.83   | 0.69~0.77  |
| $m_r$                   | -         | 0.45~0.47  | -           | 0.77~0.80  |
| $\Delta h/U^2$          | 0.08~0.10 | 0.08~0.095 | 0.107~0.117 | 0.08~0.115 |
| No. of stall cells      | 1         | 1          | 1           | 1          |
| Rotating speed of cells | 62.5%     | 68.7%      | 58.1%       | 59.4%      |

and the shape of pressure histories is well-matched to the experimental ones. At 95% speed, the rotating speed of the stall cell in the computation has a good agreement to the experiment, and the fluctuation amplitude is also comparable.

**Figure 5** shows a zoom of the experimental time histories at 60% speed at approximately 100 revolutions after stall inception, where a distinct change in the fluctuations caused by the rotating stall transitioning from one stall cell to two takes place. This transition is unusual with previous fans typically only showing a one cell pattern rotating at about 60% of the fan speed. Here, after transition to two stall cells, the rotational speed of the cells remains unchanged around 60% and the fluctuation amplitude does not change significantly. The reason for the dividing of the stall cell is unknown and work is now continuing with the simulation to investigate whether this division of the stall cell can be captured numerically or not. (It may take two or three months with 48 CPUs to obtain numerical results for another 100 revolutions.)

**Table 2** shows the comparison of flow quantities in a fully-developed rotating stall after the stall has had enough time to develop to a stable pattern. The mass flow rate calculated from the pressures ( $m_p$ ) is well-matched to each other at both fan speed, although the mass flow rate calculated from the mass flux ( $m_r$ ) at 60% speed in the computation is significantly different from the experimental value, as mentioned above. The values of  $\Delta h/U^2$  obtained from the numerical results show a

good agreement with the experimental values. There is also good agreement in the number and rotational speed of stall cells between the experiment and computation. This table clearly shows that the numerical method, including boundary conditions and stall triggering method, used in this study can generate realistic flow data under rotating stall.

### Internal flow

The instantaneous static pressure upstream of the fan is shown in **Fig. 6** during stall initiation and development for 60% speed. Due to the mis-staggered blade, the flow is intrinsically asymmetric from the beginning of the unsteady flow simulation. It is evident that a small disturbance arises from the mis-staggered blade, shown in **Fig. 6(a)**, and it makes small ticks in the static pressure histories in **Fig. 3** even before stall initiation. The disturbance grows bigger up to a critical size for the first 4 revolutions, and it then starts moving in the counter-clockwise direction along the annulus, appearing as a growing stall cell around 5 revolutions in the pressure histories (**Fig. 6(b)**). After stall initiation, several other small disturbances appear in the flow field, rotating along the annulus with different rotating speed (**Fig. 6(c)**). Thereafter, these small stall cells merge together to form a single large stall cell after 12 revolutions and the stall pattern does not change significantly up to 24 revolutions, as shown in **Fig. 6(d)**.

At 95% speed, the overall features are similar to the 60% speed case, as shown in **Fig. 7**. A local disturbance is generated from the mis-staggered blade, grows bigger at a fixed position

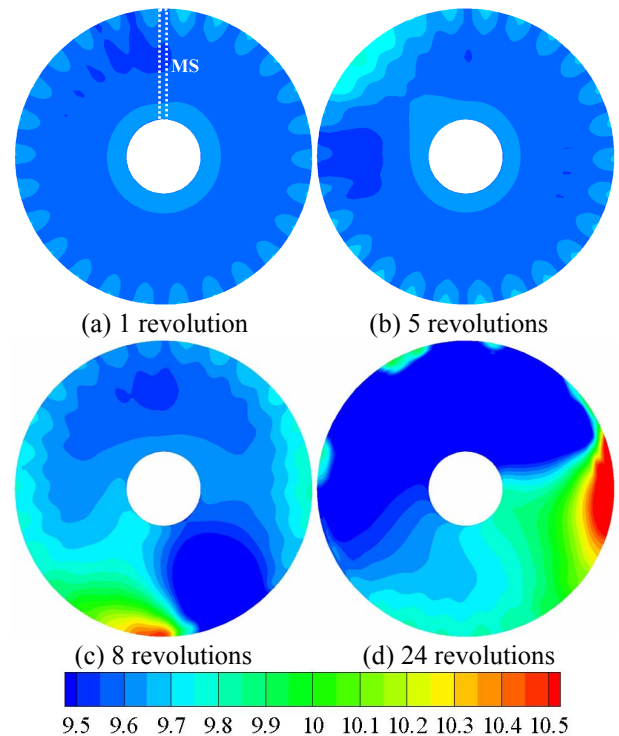


**Fig. 6 Static pressure distribution at 1.75 axial chord upstream of fan for 60% speed**

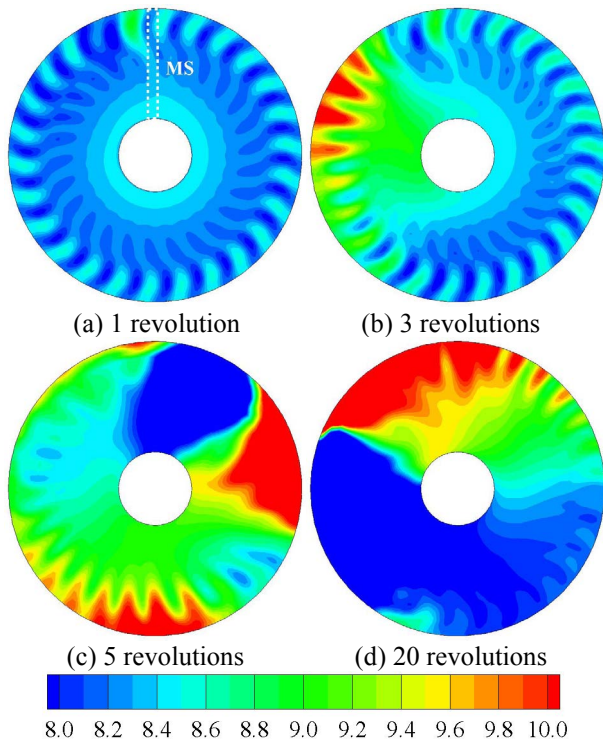


**Fig. 7 Static pressure distribution at 1.75 axial chord upstream of fan for 95% speed**

around the mis-staggered blade, and starts moving in the circumferential direction when it reaches a critical size. The rotating stall changes to a large stall cell after small cells have merged. The reverse flow region for both speeds is confined to a region near the casing with the current high aspect ratio and low hub-tip ratio of the fan.

Regardless of the fan speed, the first stall cell grows from the mis-staggered blade so rotating stall always initiates with a small disturbance at the same rotor position. This finding is consistent with the experimental work of Day [1]. In his experiment, a spike-type stall inception started near the same location. It is believed that the local disturbance caused by an external disturbance, especially a blade with different stagger or tip gap, may be connected to spike-type stall inception. In order to prove this conjecture rigorously, a more sophisticated numerical method like LES (large eddy simulation) with finer grids and time steps is essential to resolve most of the small disturbances existing in the flow fields of the whole fan. However, this is a daunting task requiring huge computational resources and it is beyond the current computational capability. There is another thing to be noted. In this test rig, the final stall pattern is the same, independent of the fan speed, with a single large stall cell formed finally. In the previous study for a real engine geometry [14], it was found that the stall pattern is considerably speed-dependent (like a core compressor) so that increasing the fan speed results in an increase in size and in a decrease in the number of stall cells. It is unclear why

geometrical factors affect speed-dependency of the stall pattern and more investigations are necessary.

**Figure 8** shows entropy distribution and instantaneous stream lines inboard of the tip (99% of span from hub) for 60% speed. The high-entropy region in the figure coincides with the tip leakage flow core and the interface between the tip leakage and main flows, where axial velocity is usually below zero. The instantaneous stream lines are used to check the spillage of the tip leakage flow. At 1 revolution, a spillage of tip leakage flow occurs around the leading edge of the trailing blade (as indicated with a red-circle). This spillage causes a small asymmetric disturbance in the pressure field of **Fig. 6(a)** and appears as a small tick (like spike) in the pressure time histories in **Fig. 3(b)**. It is evident that the interface of the tip leakage and main flows is locally perpendicular to the axial direction just before this moment and this is consistent with the observation of Hoying et al. [7]. The mechanism for the spillage can be found in Choi et al [14] and is described as follows. “The increased incidence of the mis-staggered blade raises the blade loading and intensifies the tip leakage flow. Then the strong tip leakage flow pushes the main flow forward and causes a spillage.” In **Fig. 8(b)**, the first spillage changes the load distribution of the trailing blade and causes another spillage, consequently the spillage being successively transferred over the blade row. The disturbance covering the trailing blades of the mis-staggered one grows bigger until it reaches a critical size as shown in **Fig. 8(c)**.

At 95% speed, the flow is supersonic and consequently, due to the existence of the detached passage shock, some different features occur (as shown in **Fig. 9**). At the beginning of unsteady simulation, a strong detached shock is still present

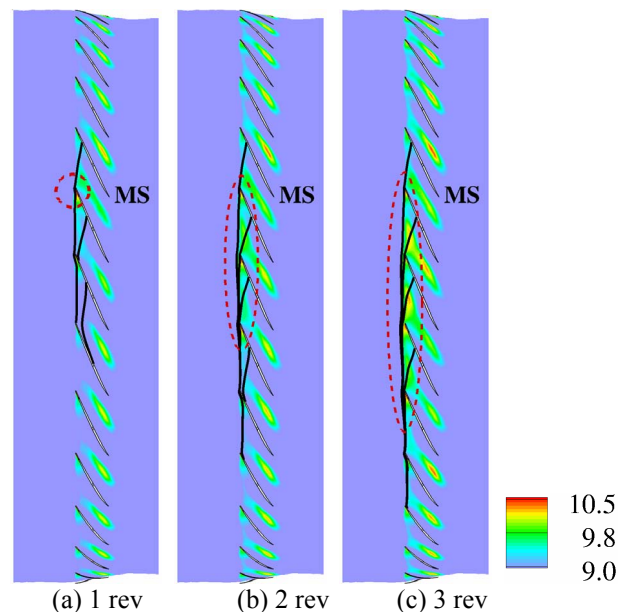


**Fig. 8 Entropy distribution and instantaneous stream lines inboard of tip (99% span from hub) for 60% speed**

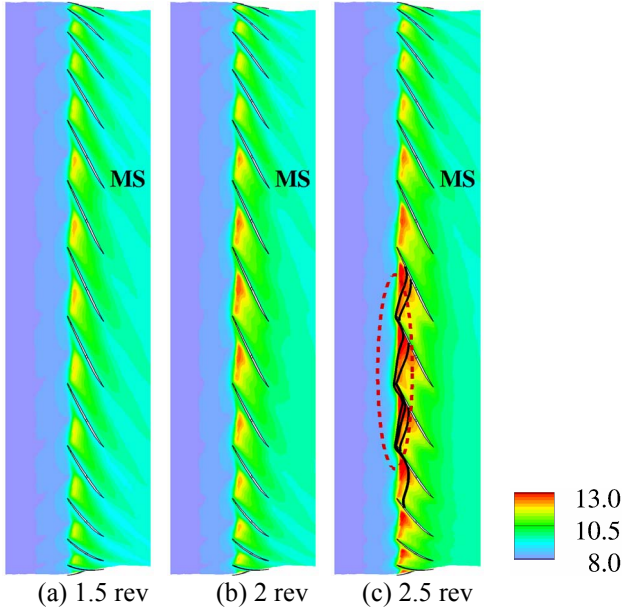


**Fig. 9 Entropy distribution and instantaneous streamlines inboard of tip (99% span from hub) for 95% speed**

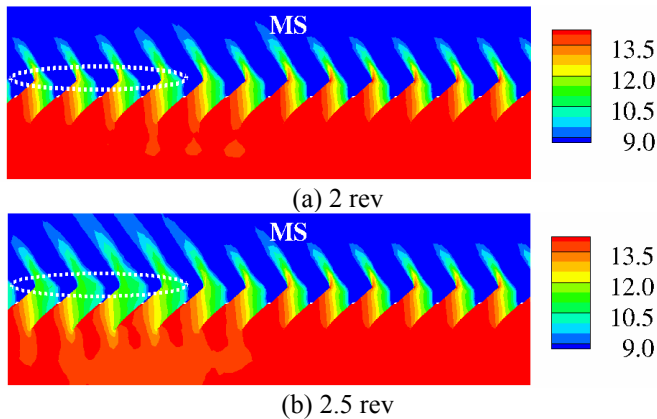


**Fig. 10 Static pressure distribution inboard of tip (99% span from hub) for 95% speed**

at the leading edge of each blade which makes a high pressure region at the leading edge of the pressure surface, pushing the tip leakage flow backward, as stated by Chen et al. [12]. Instead of spilling, the tip leakage flow accumulates on the pressure side of the trailing blade and increases the blade loading, consequently intensifying the tip leakage flow of the trailing blade. This process occurs successively, forming small disturbances over the trailing blades as shown in **Fig. 9(a)**. At 2 revolutions, the asymmetric disturbance grows over the trailing blades to block the main flow but there is still no spillage, as shown in **Fig. 9(b)**. At this instant, the shock is still strong enough to keep the leakage flow from spilling around the trailing blade, as shown in **Fig. 10(a)**. The disturbance grows bigger as the mass flow rate decreases, weakening the detached passage shock. When the shock is weak enough, the high

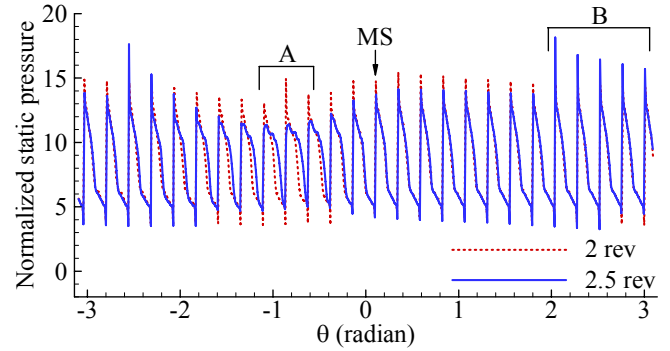
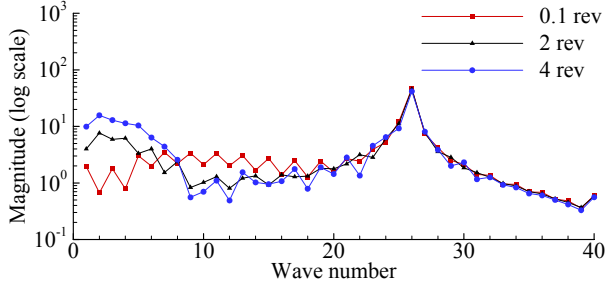


**Fig. 11 Static pressure variation across blade inboard of tip for 95% speed**

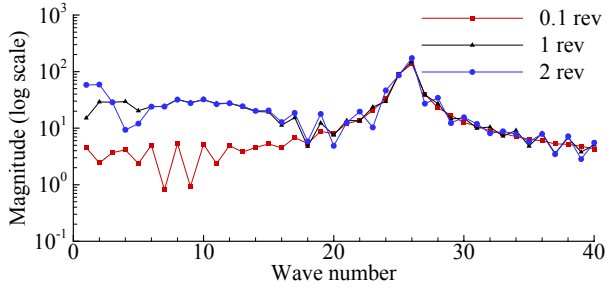
pressure region at the trailing blades disappear (at the white-circle in **Fig. 10(b)**) and the spillage occurs at the same time around the leading edges of several blades (indicated with the red circle in **Fig. 9(c)**). At this moment, a growing stall cell starts to appear in the pressure time histories of **Fig. 4(b)**. However, the shock on the leading blade is still strong enough to avoid spillage in this region. It is clear that the spillage of tip leakage flow occurs prior to spike-type stall inception, regardless of fan speed, and this is consistent with observations of Vo et al. [10].

**Figure 11** shows static pressure variation along the line through the highest pressure region generated by the detached shock at 95% speed on the pressure surface near the leading edge. The high pressure peaks are on the pressure surfaces, while the low pressure peaks are on the suction surfaces. At 2 revolutions, the detached passage shocks of the trailing blades start weakening after an asymmetric disturbance is formed, although their strength is still comparable to the others. As the disturbance is growing, the high pressure peaks of the trailing blades decrease very quickly (in 0.5 revolution), causing the spillage of tip leakage flows (**A**), while those of the leading blades do not change significantly. Especially, the shocks of the diametrically opposite blades (**B**) to the spilled blades become stronger than ever due to the displaced flow caused by the blockage of the disturbance. These results show the detached passage shock is closely related to the stall inception in a transonic or supersonic flow regime. Based on this result, it might be possible to detect stall inception (or spillage) in a transonic compressor using static pressure tapping on the pressure surface near the leading edge instead of upstream sensors.

**Figure 12** shows spatial Fourier components of the instantaneous static pressure around the annulus upstream of the fan at three instants before stall inception. The mass flow rate at all instants is slightly smaller than the value at the beginning of the unsteady computation. The most dominant harmonic in all cases is the 26<sup>th</sup> mode, the blade passing harmonic, caused by a periodic pressure variation which has the same length scale as the rotor pitch. At 0.1 revolutions, there are also weaker but recognizable modes present. At 60% speed, the magnitude of the first 6 modes begins to increase



(a) 60% speed



(b) 95% speed

**Fig. 12 Fourier components of casing static pressure at inlet before stall inception**

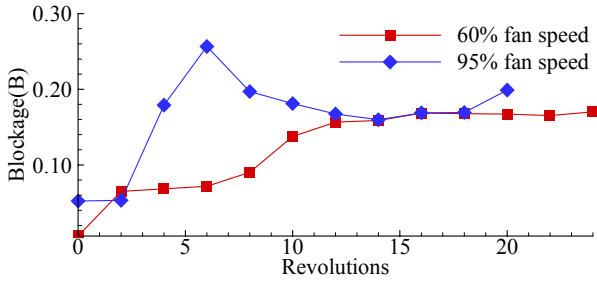


**Fig. 13 Blockage variation**

after 2 revolutions, with the second mode being the most dominant. The magnitude of these modes has increased further at four revolutions. At 95% speed, the modes longer than the 18<sup>th</sup> increase simultaneously after 1 revolution, and thereafter the first and second modes grow rapidly. At both speeds, prevailing modes are the first and the second ones as the disturbance grows bigger. This observation is also supported by the results of Chen et al. [12] in which the first mode grows persistently during the pre-stall stage.

The stall blockage effect can be defined as

$$B = \int_{A_b} \left(1 - \frac{\rho u}{\rho u}\right) \cdot dA / A_e \quad (2)$$

where the integration is performed over the blocked region, in which the mass flux ( $\rho u$ ) is smaller than the area-averaged mass flux ( $\bar{\rho u}$ ). The calculated blockage at each instant is shown in

**Fig. 13.** At 95% fan speed, the blockage increases rapidly for the first 4 revolutions after stall initiation, and reaches a maximum value at 6 revolutions and decreases slowly thereafter. This blockage variation is closely connected to the

mass flow rate variation and the stall pattern. In the previous study of Choi et al. [14], it was shown that the blockage has a maximum value when the blocked region exhibits a thick band near the casing after stall inception, and it decreases as the small stall cells merge together to form larger cells at higher rotational speeds. The blockage variation for 60% speed exhibits different features from the 95% speed case. The blockage increases slowly as the small disturbance grows from the mis-staggered blade, to reach a maximum around 12 revolutions and remain unchanged thereafter because the stall pattern does not change significantly after this moment. For this fan, regardless of fan speeds, the blockage has nearly the same value after rotating stall is fully-developed, as the stall patterns are very similar.

### Mass flow measurement accuracy

**Figure 14** shows the difference between  $m_r$  and  $m_p$  and both values are obtained from the numerical data. Before stall initiation, the ratio of  $m_p$  to  $m_r$  is nearly one, implying that there is no significant difference between the two methods of calculation. At 95% speed, this ratio decreases very sharply in three revolutions after stall initiation due to the strong reversal flow caused by small stall cells (**Fig. 7(c)**), but it recovers shortly after to 90% of its original value. However, at 60% speed, the difference grows to be 30% between  $m_r$  and  $m_p$  after stall inception and keeps its value after stall development. There are two things to be noted. Firstly, the mass flow rate obtained by the casing pressure ( $m_p$ ) is incorrect in the transient flow, especially at the higher fan speed. Secondly, after the stall cell has had enough time to develop, the difference in two mass flow rates is much larger in the lower speed than in the higher speed. This is connected to the extent of upstream region affected by stall cells and will be discussed next paragraph.

**Figure 15** shows the non-dimensional entropy distribution on the casing at 24 and 20 revolutions for 60% and 95% fan speeds respectively. The black line indicates the location of the static pressure measurement from the numerical data for the mass flow calculation. Under fully-developed rotating stall, the high-entropy region coincides with the reversal flow region. In both cases, there is a single large stall cell dominating the flow field in the fan blade row, causing a large loss. The axial extent of the stall cell has extended 5.0 axial chord at 95% speed and 3.9 axial chord at 60% upstream of fan blades. In front of the measurement plane, the high-entropy region at 95% speed has a circumferentially narrow region (just over one-third of the blade row), while the region at 60% speed spreads over two-third of the whole annulus. This helps explain why if the mass flow rate is calculated from the casing pressures at the measurement plane, the stall cell at 60% speed affects the results more significantly than the 95% case, causing 30% difference between  $m_p$  and  $m_r$  in **Fig. 14**.

The problem in the experiment is the location of the Kulites measuring the casing static pressure for the mass flow rate calculation, which are positioned too close to the fan blade, so that the stall cell has a significant effect on the pressure

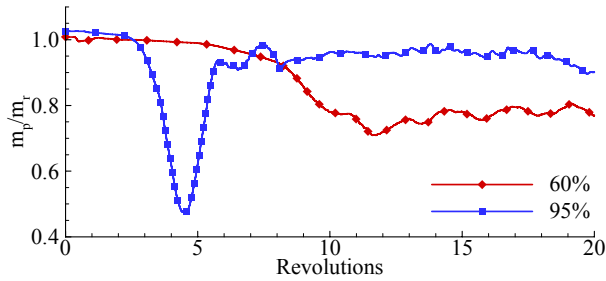


**Fig. 14 Mass flow rate difference caused by calculation method**

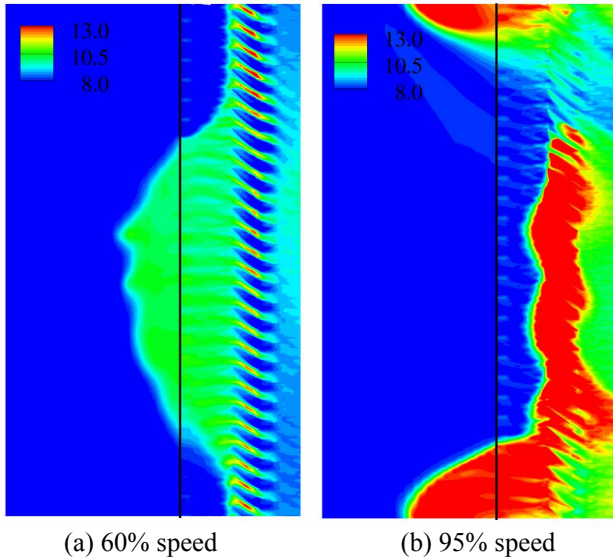


**Fig. 15 Entropy distribution on casing**

measurement. The assumption of uniform flow field is not valid in rotating stall. To avoid the error in the mass flow rate measurement, the pressure sensors should be moved further upstream of the fan, where the effect of stall cells cannot be felt.

## CONCLUDING REMARKS

Using an advanced numerical method, stall simulations were conducted for two different fan speeds and the numerical results were also compared to the experimental data for validation. The following conclusions can be made from the numerical and experimental results.

1. The flow variables obtained from the numerical results are well-matched to the experimental values in the mass flow rate, loading parameter, stall cell number and speed of stall cells under fully-developed rotating stall. This comparison definitely shows that the numerical method is accurate enough to be used to predict the flow phenomena under rotating stall.
2. In the experiment, pressure sensors for mass flow measurement should have been placed further upstream of the fan blade to avoid the effects of the transient flow. In

this work, a single large stall cell affects up to 5.0 axial chord upstream of the fan. The pressure sensors mounted close to the fan blade result in inaccurate mass flow rate during stall experiments.

3. An initial small disturbance over few blades is originated from the mis-staggered blade and appears as a small tick (like spike) in the pressure histories. After growing to reach a critical size, the disturbance starts to move in the circumferential direction and becomes a rotating stall cell. It is believed that the above scenario for stall inception might be connected to the experimentally observed spike-type stall inception.
4. At the lower speed (subsonic), tip leakage flow spillage occurs successively in the trailing blades of the mis-staggered blade and generates an initial disturbance growing to be a stall cell. However, at 95% speed (supersonic) the strong detached shock initially stops the tip leakage flow spilling around the trailing blade. When the passage shock becomes weak enough, the flow spillage starts and develops into the stall cell.

## ACKNOWLEDGMENTS

The authors would like to thank EPSRC for funding the work and Rolls-Royce plc. for providing data and allowing its publication. They would also like to thank their colleague Prof. Nick Cumpsty at Imperial College for many very useful discussions.

## NOMENCLATURE

|          |   |
|----------|---|
| $A_b$    | Blocked region  |
| $A_e$    | Exit area   |
| $B$      | Blockage  |
| $C_x$    | Axial chord length                                    |
| $MS$     | Mis-staggered blade                                   |
| $h$      | Entropy   |
| $m_p$    | Mass flow rate calculated from casing static pressure |
| $m_r$    | Mass flow rate calculated from mass flux              |
| $P_0$    | Inlet total pressure                                  |
| $p$      | Static pressure                                       |
| $R$      | Gas constant  |
| $T_0$    | Inlet total pressure                                  |
| $U$      | Tip rotational speed                                  |
| $u$      | Axial velocity  |
| $\theta$ | Circumferential position                              |
| $\gamma$ | Specific heat ratio                                   |
| $\rho$   | Air density   |

## REFERENCES

- [1] Day, I. J., 1993, "Stall Inception in Axial Compressors," *ASME J. Turbomach.*, **115**, pp. 1-9.
- [2] Day, I. J., 1993, "Active Suppression of Rotating Stall and Surge in Axial Compressors," *ASME J. Turbomach.*, **115**, pp. 40-47.

- [3] Camp, T. R., and Day, I. J., 1998, "A Study of Spike and Modal Stall Phenomena in a Low-Speed Axial Compressor," *ASME J. Turbomach.*, **120**, pp. 393-401.
- [4] Freeman, C., Wilson, A. G., Day, I. J., and Swinbanks, M. A., 1998, "Experiments in Active Control of Stall on an Aeroengine Gas Turbine," *ASME J. Turbomach.*, **120**, pp. 637-647.
- [5] Day, I. J., Breuer, T., Escuret, J., Cherett, M., and Wilson, A., 1999, "Stall Inception and the Prospects for Active Control in Four High-Speed Compressors," *ASME J. Turbomach.*, **121**, pp. 18-27.
- [6] He, L., 1997, "Computational Study of Rotating-Stall Inception in Axial Compressor," *AIAA J. Propul. Power*, **13**, pp. 31-38.
- [7] Hoying, D. A., Tan, C. S., Vo. H. D., and Greitzer, E. M., 1999, "Role of Blade Passage Flow Structures in Axial Compressor Rotating Stall Inception," *ASME J. Turbomach.*, **121**, 735-742.
- [8] Gourdain, N., Burguburu, S., Leboeuf, F., and Miton, H., 2006, "Numerical Simulation of Rotating Stall in a Subsonic Compressor," *Aerosp. Sci. Technol.*, **10**, pp. 9-18.
- [9] Choi, M., Baek, J. H., Oh, S. H., and Ki, D. J., 2008, "Role of Hub-Corner-Separation on Rotating Stall in an Axial Compressor," *Trans. Japan Soc. Aero. Space Sci.*, **51**, pp. 93-100.
- [10] Vo, H. D., Tan, C. S., and Greitzer, E. M., 2008, "Criteria for Spike Initiated Rotating Stall," *ASME J. Turbomach.*, **130**, 011023.
- [11] Vahdati, M., Simpson, G., and Imregun, M., 2008, "Unsteady Flow and Aeroelasticity Behavior of Aeroengine Core Compressors During Rotating Stall and Surge," *ASME J. Turbomach.*, **130**, 031017.
- [12] Chen, J.-P., Hathaway, M. D., and Herrick, G. P., 2008, "Prestall Behavior of a Transonic Axial Compressor Stage via Time-Accurate Numerical Simulation," *ASME J. Turbomach.*, **130**, 041014.
- [13] Choi, M., Vahdati, M., and Imregun, M., 2009, "Numerical Strategies for Capturing Rotating Stall," *Proceedings of ISUAAAT12*, Paper No. I12-S6-4.
- [14] Choi, M., Vahdati, M., and Imregun, M., 2011, "Effects of Fan Speed on Rotating Stall Inception and Recovery," *ASME J. Turbomach.*, **133** (in press)
- [15] Gourdain, N., Burguburu, S., Leboeuf, F., and Michon, G. J., 2010, "Simulation of Rotating Stall in a Whole Stage of an Axial Compressor," *Compu. Fluids*, **39**(9), pp. 1644-1655.
- [16] Anderson, S. J., and Smith, N. H. S., 2003, "Analysis of Unsteady Casing Pressure Measurements During Surge and Rotating Stall," *Proceedings of ISUAAAT10* (Paper No. is unavailable.)
- [17] Sayma, A. I., Vahdati, M., Sbardella, L., and Imregun, M., 2000, "Modeling of 3D Viscous Compressible Turbomachinery Flows Using Hybrid Grids," *AIAA J.*, **38**(6), pp. 945-954.
- [18] Vahdati, M., Sayma, A., Freeman, C., and Imregun, M., 2005, "On the Use of Atmospheric Boundary Conditions for Axial-Flow Compressor Stall Simulations," *ASME J. Turbomach.*, **127**(3), pp. 349-351.